#### **OPEN ACCESS**



# JWST/NIRCam Imaging of the Bipolar Planetary Nebula NGC 6537: The (Infra)red Spider, Revealed

Joel H. Kastner 1,2,3 , Paula Moraga Baez 2,3,4 , Bruce Balick b, Rodolfo Montez, Jr. 6 , Caroline Gieser b, Mikako Matsuura b, Jason Nordhaus 2,9 , and Miguel Santander-Garcia 10 , Mikako Matsuura b, Jason Nordhaus 2,9 , and Miguel Santander-Garcia 10 , Mikako Matsuura b, Jason Nordhaus 2,9 , and Miguel Santander-Garcia 10 , Mikako Matsuura b, Jason Nordhaus 2,9 , and Miguel Santander-Garcia 10 , Mikako Matsuura b, Jason Nordhaus 2,9 , and Miguel Santander-Garcia 10 , Mikako Matsuura b, Jason Nordhaus 2,9 , and Miguel Santander-Garcia 10 , Mikako Matsuura b, Jason Nordhaus 2,9 , and Miguel Santander-Garcia 10 , Mikako Matsuura b, Jason Nordhaus 2,9 , and Miguel Santander-Garcia 10 , Mikako Matsun b, Jason Nordhaus 2,9 , and Miguel Santander-Garcia 10 , Mikako Matsuner britted to Technology, Rochester, NY 14623, USA 4 , Department of Physics and Astronomy, University of Western Ontario, London, ON N6A 5B7, Canada 5 , Department of Astronomy, University of Washington, Seattle, WA 98195, USA 6 , Center for Astrophysics | Harvard & Smithsonian, Cambridge, MA 02138, USA 7 , Max-Planck-Institut für Astronomie, Königstuhl 17, D-69117 Heidelberg, Germany 8 , Cardiff Hub for Astrophysics Research and Technology (CHART), School of Physics and Astronomy, Cardiff University, The Parade, Cardiff CF24 3AA, UK 9 , National Technical Institute for the Deaf, Rochester Institute of Technology, Rochester, NY 14623, USA 10 , Observatorio Astronómico Nacional, C/ Alfonso XII 3&5, E-28014 Madrid, Spain Received 2025 August 14; revised 2025 September 13; accepted 2025 September 13; published 2025 October 28

#### **Abstract**

We present James Webb Space Telescope (JWST) Near-Infrared Camera (NIRCam) Brα, H<sub>2</sub>, [Fe II], and polycyclic aromatic hydrocarbon (PAH) imaging of the molecule-rich, high-excitation bipolar planetary nebula (PN) NGC 6537 (the Red Spider), complemented by new Atacama Large Millimeter/submillimeter Array (ALMA) and Chandra X-ray Observatory (Chandra) observations and archival Hubble Space Telescope (HST) images. The resulting multiwavelength view of the Red Spider establishes the detailed lobe-torus structure of the nebula and the mass-loss history of its progenitor star. The extinction-penetrating JWST/NIRCam Br $\alpha$  and PAH and ALMA 3 mm continuum imaging exposes the complexity of the ionized inner nebula. JWST/NIRCam H<sub>2</sub> imaging traces the full,  $\sim 1.1$  pc extent of the bubble-like lobes formed by fast ( $\sim 300-400$  km s<sup>-1</sup>) polar outflows, while ALMA  $^{13}$ CO(1–0) mapping reveals a point-symmetric, slowly ( $\sim$ 10 km s<sup>-1</sup>) expanding equatorial torus of radius  $\sim 0.13$  pc. In striking contrast, the [Fe II] image displays an extended S-shaped emission morphology that traces collisions between an active, collimated wind and slower-moving material along the lobe rims. No X-rays are detected from the nebula or its central star in deep Chandra/HRC-I imaging. However, the combined HST and JWST imaging reveals a near-IR excess at the central star indicative of emission from hot (~1000 K) circumstellar dust. We propose that interactions between the nebular progenitor star and a close companion are responsible for the ejection of NGC 6537's molecular torus, the formation of a circumbinary dust disk, and the launching of fast, wandering, collimated outflows that have inflated the polar lobe bubbles traced by near-IR H<sub>2</sub> emission and are presently generating the [Fe II]-emitting shocks.

Unified Astronomy Thesaurus concepts: Planetary nebulae (1249); Stellar winds (1636); Stellar jets (1607)

# 1. Introduction

The planetary nebula (PN) NGC 6537 is an archetype of the class of extreme high-excitation, yet highly molecule-rich, bipolar nebulae. This elite PN class includes both dynamically young objects such as NGC 7027, NGC 6302, Hubble 5, NGC 2440, and NGC 6445, and dynamically older PNe, such as NGC 2818 and NGC 2899, all of which are characterized by the presence of dusty, pinched waists and high-velocity polar outflows (J. Bublitz et al. 2023; J. Kastner et al. 2023; P. Moraga Baez et al. 2023, 2025, and references therein). Despite their large masses of molecular gas, these objects harbor some of the hottest and most luminous known PN central stars, with effective temperatures of  $\sim$ 150–250 kK and luminosities of  $\sim$ 10<sup>3</sup>–10<sup>4</sup>  $L_{\odot}$ . The profound departures from spherical symmetry of such PNe defy the standard model of PNe as the products of single stars that have completed their asymptotic giant branch (AGB) evolution with the ejection of their H-rich envelopes, exposing their hot cores en route to becoming white dwarfs. Instead, the axisymmetric and

Original content from this work may be used under the terms of the Creative Commons Attribution 4.0 licence. Any further distribution of this work must maintain attribution to the author(s) and the title of the work, journal citation and DOI.

point-symmetric density structures that characterize moleculerich bipolar PNe are indicative of the presence of close, interacting binary companions (e.g., O. De Marco 2009; D. Jones & H. M. J. Boffin 2017; J. H. Kastner et al. 2022, and references therein).

Various models of the structural evolution of bipolar PNe, ranging from schematic to highly detailed, have been developed over the past four decades (see, e.g., M. Morris 1987; B. Balick & A. Frank 2002; B. Balick et al. 2019, and references therein). Most such models invoke either the formation of an accretion disk around the secondary star in a detached binary configuration with the mass-losing (PN-generating) AGB or post-AGB primary star (e.g., M. Morris 1987; N. Soker & M. Livio 1994; N. Soker & S. Rappaport 2000; R. Sahai et al. 2016; Z. Chen et al. 2017; P.-S. Huang et al. 2020), or the onset of common envelope evolution in a closer initial binary configuration (e.g., G. García-Segura et al. 2018, 2022; Y. Zou et al. 2020). However, direct evidence of binary companions to the central stars of high-excitation, molecule-rich bipolar PNe like NGC 6537 remains elusive, due to the bright, morphologically complex core regions of such PNe and the large luminosities of their post-AGB (pre-white-dwarf) central stars.

NGC 6537 has long been the subject of various groundbased optical imaging and spectroscopic studies aimed at understanding its structure, excitation, composition, and kinematics (e.g., W. Feibelman et al. 1985; R. L. M. Corradi & H. E. Schwarz 1993; L. Cuesta et al. 1995; L. H. Aller et al. 1999). In optical emission-line and near-IR H<sub>2</sub> imaging, the nebula displays a bright, compact core region with a pair of protruding, limb-brightened polar lobes, each extending over  $\sim 1'$  (R. L. M. Corradi & H. E. Schwarz 1993; J. H. Kastner et al. 1996; M. Matsuura et al. 2005). This morphology, as captured in a color rendering of Hubble Space Telescope (HST) optical imaging of the nebula, earned NGC 6537 its "Red Spider" nickname. 11 The distance to NGC 6537 is poorly determined, with literature estimates ranging from  $D \sim 0.9$  to 2.4 kpc (M. Matsuura et al. 2005); in this paper, we adopt the estimate  $D = 1.8 \pm 0.5$  kpc (D. J. Frew et al. 2016).

The long-slit spectroscopy of R. L. M. Corradi & H. E. Schwarz (1993) and L. Cuesta et al. (1995) revealed (deprojected) expansion speeds of  $\sim$ 300–400 km s<sup>-1</sup> along the nebula's polar axis, and constrained the polar axis inclination to lie in the range  $\sim 30^{\circ}$  –  $40^{\circ}$  with respect to the plane of the sky. L. Cuesta et al. (1995) also found spectroscopic evidence for expansion velocities at the nebular core that are both far higher ( $\sim$ 2000 km s<sup>-1</sup>) and much lower ( $\sim$ 18 km s<sup>-1</sup>) than those of the polar lobes, and modeled the ionized gas kinematics in terms of a disk-lobe structure. The notion of a system of polar lobe shocks in the model presented by L. Cuesta et al. (1995) is supported by the nature of certain glaring deficiencies in photoionization modeling of the nebula (L. H. Aller et al. 1999), although the large "disk" in this model is perhaps better termed a "torus" given this large, dense, equatorial structure was not hypothesized to be in Keplerian rotation.

Many parallels between NGC 6537 and the intensively studied bipolar PN NGC 6302 have been described in the literature over the past four decades; indeed, the two have frequently been the subjects of observations reported and analyzed in the same paper. Both nebulae are often cited as classical examples of Peimbert Type I PNe, i.e., the N-rich descendants of relatively high-mass ( $\sim 3-8~M_{\odot}$ ) progenitor stars (e.g., C. Quireza et al. 2007). M. C. B. Ashley & A. R. Hyland (1988) obtained detections of 1.96  $\mu$ m [Si VI] emission for both PNe, implying very high central star effective temperatures in both cases. N. Rowlands et al. (1994) and S. Casassus et al. (2000) presented detections and analysis of numerous additional coronal (forbidden, highionization-state) IR lines from Infrared Space Observatory and ground-based spectroscopy, respectively, of both nebulae. S. Casassus et al. (2000) used their results to deduce central star effective temperatures of ~240 kK for NGC 6302 and ~160 kK for NGC 6537, and obtained luminosity estimates of 8500  $L_{\odot}$  for both stars. On the basis of the detection of the central star of NGC 6537 in HST imaging, M. Matsuura et al. (2005) obtained estimates for the effective temperature and luminosity consistent with those inferred by S. Casassus et al. (2000), albeit with much larger ranges of uncertainty in both parameters.

The millimeter-wave molecular line surveys of NGC 6537 by J. L. Edwards & L. M. Ziurys (2013) and NGC 6302 by P. Moraga Baez et al. (2023, 2025) have established the extraordinarily rich molecular chemistry of both nebulae. In particular, both studies yielded numerous detections of N- and S-bearing molecules, indicative of the products of nucleosynthesis in the relatively massive progenitors of these PNe. Interferometric mapping by the Atacama Large Millimeter/submillimeter Array (ALMA) demonstrates that, in both cases, the molecular gas is confined to dense, dusty equatorial tori expanding at  $\sim 10$ –20 km s<sup>-1</sup> (P. Moraga Baez et al. 2023, 2025). On the basis of coherent submillimeter polarization signatures, indicative of large-scale dust grain alignments, L. Sabin et al. (2007) found evidence for toroidal magnetic fields threading the dusty waists of both nebulae.

In this paper, we present a new observational study of NGC 6537 with the Near-Infrared Camera (NIRCam) on board the James Webb Space Telescope (JWST), augmented by new observations with the Chandra X-ray Observatory (Chandra) as well as archival ALMA and HST data. The new JWST/ NIRCam images of NGC 6537, combined with archival HST imaging, reveal the PN's detailed molecular and ionized gas and dust structures and the optical-near-IR spectral energy distribution (SED) of its central star, while the ALMA millimeter-wave mapping traces the ionized versus neutral gas stratification and the kinematics of the dense regions in and around the bright core of NGC 6537. The Chandra observations are aimed at detecting X-rays from energetic shocks resulting from collisions between the fast ( $\sim$ 300–400 km s<sup>-1</sup>) collimated winds from the vicinity of the central star and slow  $(\sim 10 \text{ km s}^{-1})$ , dense, "fossil" AGB winds (e.g., J. H. Kastner et al. 2012, and references therein), as well as to constrain the coronal activity of a potential companion to the central star (e.g., R. Montez et al. 2015, and references therein). We combine the results of these multiwavelength observations of NGC 6537, which span six decades of the electromagnetic spectrum, to elucidate the structure and formation of the Red Spider Nebula and the nature of its progenitor star, so as to understand the origin and evolution of molecule-rich, highexcitation PNe more generally.

The JWST and Chandra observations and archival data sources are described in Section 2. The JWST images and multi-wavelength (JWST + ALMA + HST) views of NGC 6537, and results derived from the imaging, are presented in Section 3. In Section 4, we discuss the insights into the structure and evolution of NGC 6537 obtained from the JWST + ALMA + HST imaging as well as hydrodynamic modeling of the formation of a bipolar PN, and we present analysis of the SED of the PN central star as yielded by the JWST + HST data. Section 5 presents a summary and conclusions.

## 2. Observations

# 2.1. JWST

JWST/NIRCam images of NGC 6537 were obtained on 2024 August 17 under JWST PID 4571 (PI: J. Kastner), as part of a joint Chandra–JWST program (see below). Images were obtained with NIRCam through filters F164N, F212N, F356W, and F405N, which isolate, respectively, [Fe II] 1.64  $\mu$ m, H<sub>2</sub> S(1) 1–0 2.12  $\mu$ m, polycyclic aromatic hydrocarbon (PAH) 3.28  $\mu$ m, and Br $\alpha$  4.05  $\mu$ m emission lines and features. The four images were obtained in pairs, using the short-

The see https://apod.nasa.gov/apod/ap980106.html. This arthropodic "Red Spider" moniker has stuck (and is included in the nebula's simbad database listing), despite NGC 6537's longstanding identification as a member of the class of pinched-waist "butterfly" nebulae (R. L. M. Corradi & H. E. Schwarz 1993).

wavelength + long-wavelength channels, via two dithered observations of NGC 6537. We employed SHALLOW2 readout with six groups per integration and one integration per exposure, and INTERMODULEX dithering with eight primary dithers. These observing parameters yielded an exposure time of 2319 s per filter.

Image processing tasks, as well as photometric and initial astrometric calibrations, were performed using standard JWST processing pipelines. Specifically, raw data products were generated from the original spacecraft telemetry using version 2024 1a of the JWST Science Data Processing subsystem. Version 1.14.0 of the JWST Science Calibration Pipeline was used to generate fully calibrated exposures and final mosaicked images for the dithered image sequences through each of the four filters. As the F356W dithered image sequence was saturated in the nebular core region after this standard pipeline processing, we reran the Science Calibration Pipeline using version 1.15.1 with the pixel ramp fitting option enabled during Level 1 processing (by setting the ramp fit parameter suppress one group to "False"). This additional processing step mitigated the saturation issues in the regions of the F356W image dominated by nebulosity, even though the core regions of field stars in the images remain

Finally, the images output by the pipeline processing just described were astrometrically calibrated using the positions of field stars included in Gaia Data Release 2. While the relative (filter-to-filter) astrometric accuracy was excellent, we found position tweaks of order  $\sim\!0.^{''}\!.5$  were necessary to bring the images into alignment with the Gaia star reference positions. We estimate the final, astrometrically calibrated images have absolute positional uncertainties of  $\sim\!0.^{''}\!.05$ .

### 2.2. Chandra X-Ray Observatory

We obtained six exposures targeting NGC 6537 with the High Resolution Camera imaging array (HRC-I) on board Chandra between 2024 October and 2025 July (ObsIDs 28002, 28736, 28737, 28738, 28739, and 31001), during Chandra Cycle 25, as part of the joint Chandra-JWST program 25200170 (PI: J. Kastner). The total Chandra/HRC-I exposure time was 76.13 ks. The resulting event data resulting from each exposure were processed through the Chandra X-ray Center's standard Chandra/HCR-I processing pipeline (version 10.13 for ObsIDs 28737 and 28738, and version 10.14.1.1 for all other ObsIDs), and each pipeline-processed event file was then subject to a hyperbolic screening algorithm to mitigate the effects of cosmic rays (R. P. Kraft et al. 2018). The six exposures were then merged. The resulting cosmicray-screened, merged (76.13 ks exposure) image yielded no detection of X-rays above the background within the area spanned by the NGC 6537 nebula in the JWST images (see Section 3.1). We discuss the significance of the X-ray nondetection of NGC 6537 in Section 3.3.3.

# 2.3. Archival HST and ALMA Data

We have made use of archival data from HST and ALMA as points of comparison with our new JWST/NIRCam near-IR imaging of NGC 6537. As noted, the HST data, obtained in 1998 with WFPC2 (PID 6502; PI: B. Balick), were included in the study of the core region of NGC 6537 by M. Matsuura et al. (2005, see their Table 1). The ALMA data were obtained

in the 3 mm region (ALMA Band 3) as part of a molecular line survey of high-mass star-forming regions (ALMA project code 2018.1.00424.S, PI: C. Gieser; C. Gieser et al. 2023), and are the subject of a forthcoming paper (P. Moraga Baez et al. 2025b, in preparation). Here, we utilize maps of 98.3 GHz continuum emission and the  $J=1\rightarrow 0$  (110.20135 GHz) rotational transition of  $^{13}{\rm CO}$ , obtained at spatial resolution of  $^{\sim}1''$  (see C. Gieser et al. 2023, for details). The  $^{13}{\rm CO}$  emission-line map was obtained with a velocity resolution of 0.664 km s $^{-1}$ , providing a data cube from which we have extracted velocity-integrated (moment 0) images over various velocity ranges of interest as well as an intensity-weighted mean velocity (moment 1) image.

#### 3. Results

# 3.1. Individual JWST/NIRCam Images: Full-field and Zoomed Views

The resulting full-field ( $\sim 150'' \times 150''$ ) JWST/NIRCam [Fe II],  $H_2$ , PAH, and  $Br\alpha$  images of NGC 6537 are displayed in Figure 1. Zoomed-in views of the JWST/NIRCam images, with fields of view of  $\sim 75'' \times 75''$  and  $\sim 30'' \times 30''$ , are presented in Figures 2 and 3, respectively. The morphology of the 4.05  $\mu m$  Br $\alpha$  image in the full-field rendering in Figure 1—with its bright core and open, limb-brightened polar lobes extending to the northeast and southwest from the core along position angle (PA)  $\sim 45^{\circ}$ , forming opposed pairs of "horns"—bears close resemblance to that seen in groundbased H $\alpha$  imaging of the nebula (e.g., L. Cuesta et al. 1995, their Figure 2). The ground-based spectroscopy has established that the northeast-directed and southwest-directed lobes (hereafter referred to as the NE and SW lobes) are directed away from and toward the observer, respectively (R. L. M. Corradi & H. E. Schwarz 1993; L. Cuesta et al. 1995).

The most immediately striking aspects of the full-field JWST/NIRCam images in Figure 1 are the detection of bubble-like polar lobe enclosures in 2.12  $\mu$ m H<sub>2</sub> emission, and the S-shaped morphology of the 1.64  $\mu$ m [Fe II] emission. The bubble-like structures imaged in H2, each of which extend  $\sim$ 100" from the nebular core region to the extreme corners of the NIRCam FOV in the H<sub>2</sub> image, were only marginally detected in previous ground-based 2.12  $\mu m$  H<sub>2</sub> imaging (J. H. Kastner et al. 1996; R. A. Marquez-Lugo et al. 2013), and do not appear as complete bubble-like structures in previous, deep ground-based and HST  $H\alpha + [NII]$  imaging (R. L. M. Corradi & H. E. Schwarz 1993; M. Matsuura et al. 2005; R. A. Marquez-Lugo et al. 2013). For our adopted distance, D = 1.8 kpc, the projected linear extent of each polar lobe as revealed in the JWST/NIRCam  $H_2$  imaging is  $\sim 0.9$  pc. The deprojected lengths are then  $\sim 1.1$  pc (assuming  $i = 38^{\circ}$ ; R. L. M. Corradi & H. E. Schwarz 1993). This implies lobe dynamical ages of ~3700 yr, given the inferred (deprojected) lobe expansion speeds of  $\sim 300 \text{ km s}^{-1}$  (R. L. M. Corradi & H. E. Schwarz 1993).

The zoomed-in ( $\sim$ 75"  $\times$  75") views in Figure 2 provide closer looks at the S-shaped [Fe II] emission morphology of the nebula and the delicate fine structures and wave-like features detected in H<sub>2</sub> emission. The profound point symmetry of the [Fe II] emission morphology, which is also seen in lower-resolution (ground-based) 1.64  $\mu$ m imaging of NGC 6537 (Y. Kim et al. 2024), is remarkably similar to that of

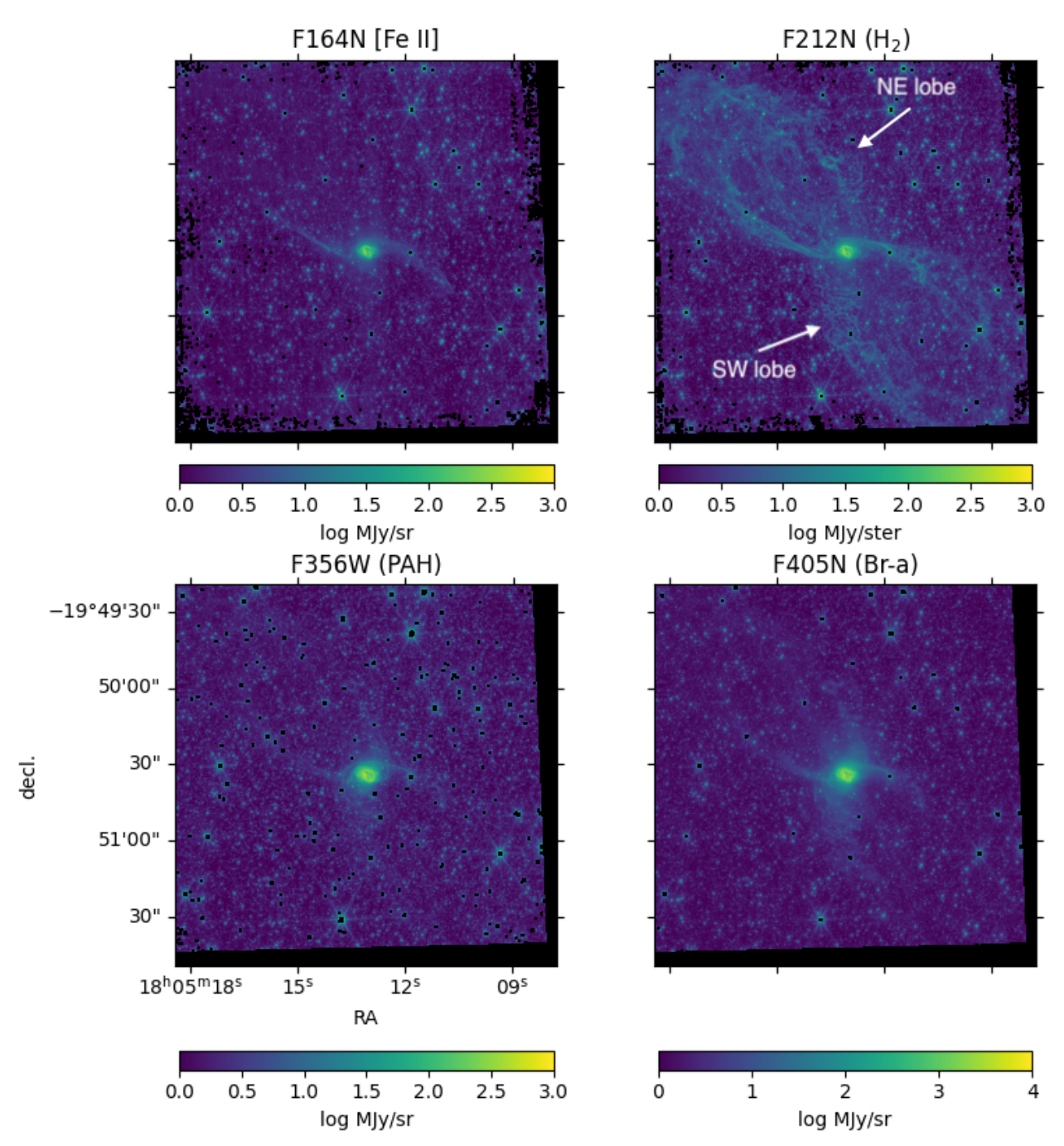


Figure 1. JWST/NIRCam images of NGC 6537, full  $150'' \times 150''$  field of view (FOV). The four image frames are arranged, from left to right and top to bottom, in the order F164N, F212N, F356W, and F405N. The rearward-facing NE and forward-facing SW polar lobes are indicated in the  $H_2$  (F212N, upper right) image.

NGC 6302, as first revealed by HST/WFC3 1.64  $\mu$ m imaging (J. H. Kastner et al. 2022). The  $\sim$ 75"  $\times$  75" frames in Figure 2 also make evident the more compact appearance of the nebula in the F356W image relative to the images in the other three filters. It is apparent from the  $\sim$ 30"  $\times$  30" image frames in Figure 3 that the fine structures seen in the F356W image just outside the bright nebular core region are similar to those imaged in H<sub>2</sub> emission. These zoomed-in views of the core region also demonstrate that NGC 6537's central star is well detected in all four NIRCam images. The  $\sim$ 30"  $\times$  30" image frames furthermore highlight the complex structure of the

nebular core region, as was also apparent in HST emission-line imaging (M. Matsuura et al. 2005).

# 3.2. JWST/NIRCam Images: Color Image Overlays

Various key features of the structure of NGC 6537 are further highlighted by the color overlays of the NIRCam images presented in Figure 4. The zoomed-in views in the middle and bottom panels make clear the apparently multilobed yet profoundly asymmetric structures within the nebular core region. The white color of the sharp-rimmed filamentary structures threading this core region in Figure 4,

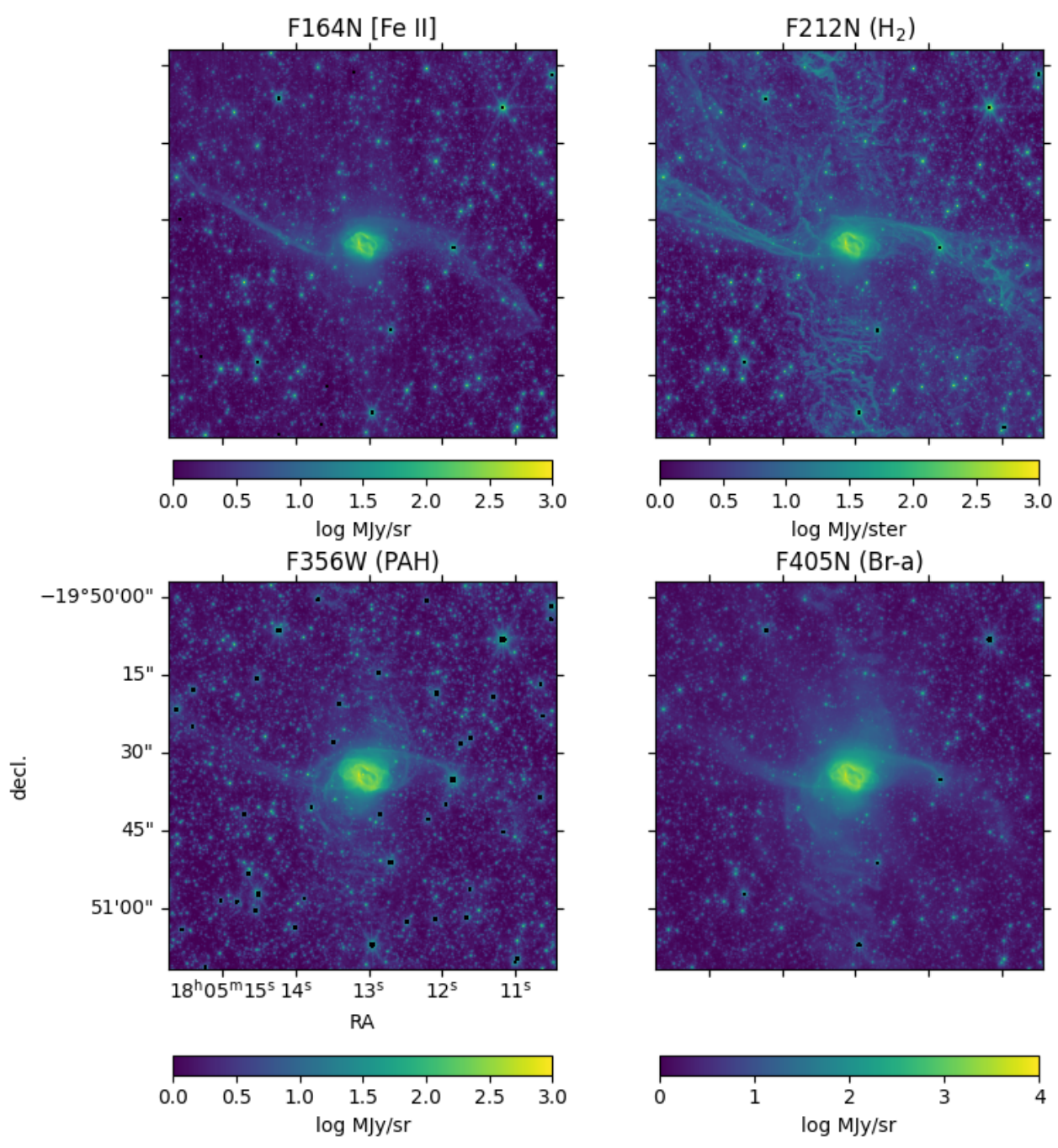


Figure 2. JWST/NIRCam images of NGC 6537 arranged as in Figure 1; zoomed-in views, 75" × 75" FOV.

best seen in the middle and bottom panels, reflects the similar intensities in the three images included in each overlay, and are hence indicative of a significant contribution of continuum (free–free) emission within the F164N, F212N, and F356W images, in the nebular core. Ground-based imaging had previously established the core region as a bright near-IR continuum source (J. H. Kastner et al. 1996), but with insufficient resolution to elucidate the fine structures threading this region. Indeed, the bright rim of near-IR continuum emission, as revealed in the zoomed-in views in Figure 4 (middle and bottom panels), appears to wrap around the central star in an irregular spiral pattern.

Note that the central star appears red in both zoomed-in color overlays in Figure 4. Given the central star's very high temperature (~160 kK; S. Casassus et al. 2000), this red color is indicative of the presence of a near-IR excess at the star that is well detected in (at least) the F356W and F405N filters (both of which are coded red in the lower panels of Figure 4). We analyze this excess quantitatively in Section 4.3.

Other differences between the NIRCam images that are highlighted in red, green, and blue in Figure 4 reveal emission in the specific line or feature lying within the filter bandpass. Thus the top panel of Figure 4 illustrates how, within both lobes, the S-shaped [Fe II]-emitting region (color coded green)

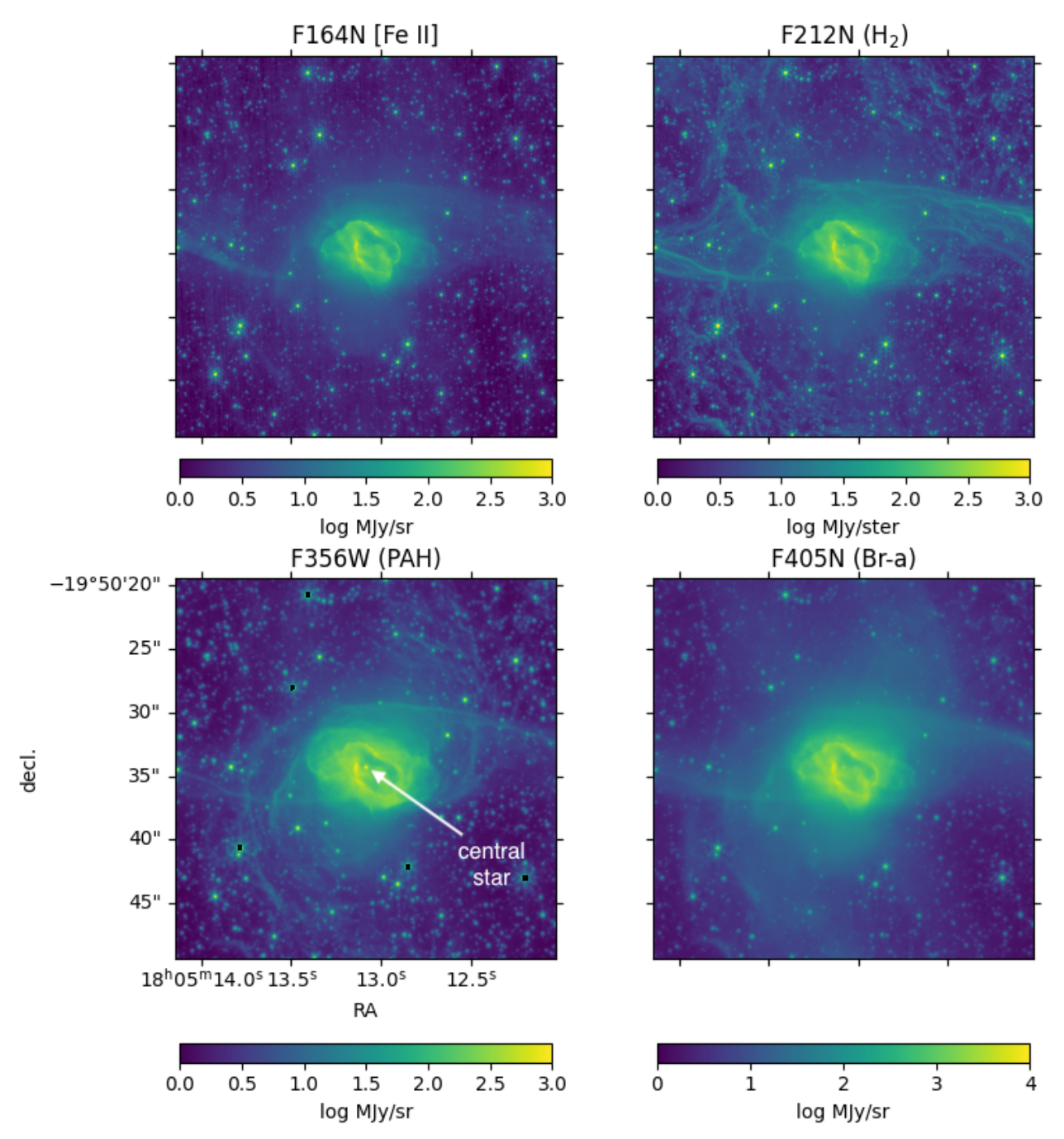


Figure 3. JWST/NIRCam images of NGC 6537 arranged as in Figure 1; zoomed-in views,  $30'' \times 30''$  FOV. The position of the central star is indicated in the PAH (F356W, lower left) image.

lies adjacent to, but offset from, the  $H_2$ -emitting lobe rims (color coded blue); more specifically, the [Fe II] is seen to trace the inner edges of the southern rim of the NE lobe and the northern rim of the SW lobe. Meanwhile comparison of the zoomed-in views of the core region in the middle and bottom panels of Figure 4 reveals a cocoon of luminous PAH emission (color coded red) surrounding the ionized nebular core (compare with Figure 8 in M. Matsuura et al. 2005). Just outside this core region, as previously noted, the PAH emission is observed to closely trace the fine filamentary structures detected in  $H_2$ ; however, the surface brightness of PAH emission drops precipitously beyond the core and inner lobe regions, while the filamentary  $H_2$  emission outlines the

full extents of the polar lobes contained within the NIRCam FOV. The vast reach of the  $H_2$  relative to the PAH emission is indicative of shock excitation for the former, versus UV excitation for the latter.

# 3.3. The JWST/HST/ALMA/Chandra Multiwavelength View of the Red Spider

## 3.3.1. The Ionized Nebular Core

Figure 5 presents a color overlay of the ALMA 3 mm continuum emission map (red) on the JWST/NIRCam 4.05  $\mu$ m Br $\alpha$  (green) and HST/WFPC2 H $\alpha$  (blue) images for the core region of NGC 6537, with the 3 mm continuum



Figure 4. Top and middle panels: wide-field ( $\sim$ 80"  $\times$  40") and zoomed-in ( $\sim$ 20"  $\times$  10") color overlays of 4.05  $\mu m$  Br $\alpha$  (red), 1.64  $\mu m$  [Fe II] (green), and 2.12  $\mu m$  H<sub>2</sub> (blue) images of NGC 6537. Bottom: the same ( $\sim$ 20"  $\times$  10") FOV as the middle panel, with the 3.56  $\mu m$  PAH image replacing Br $\alpha$  in the red channel. Images are displayed in log scale, with min and max intensities as in Figure 1, with further enhancements to highlight emission outside the core regions.

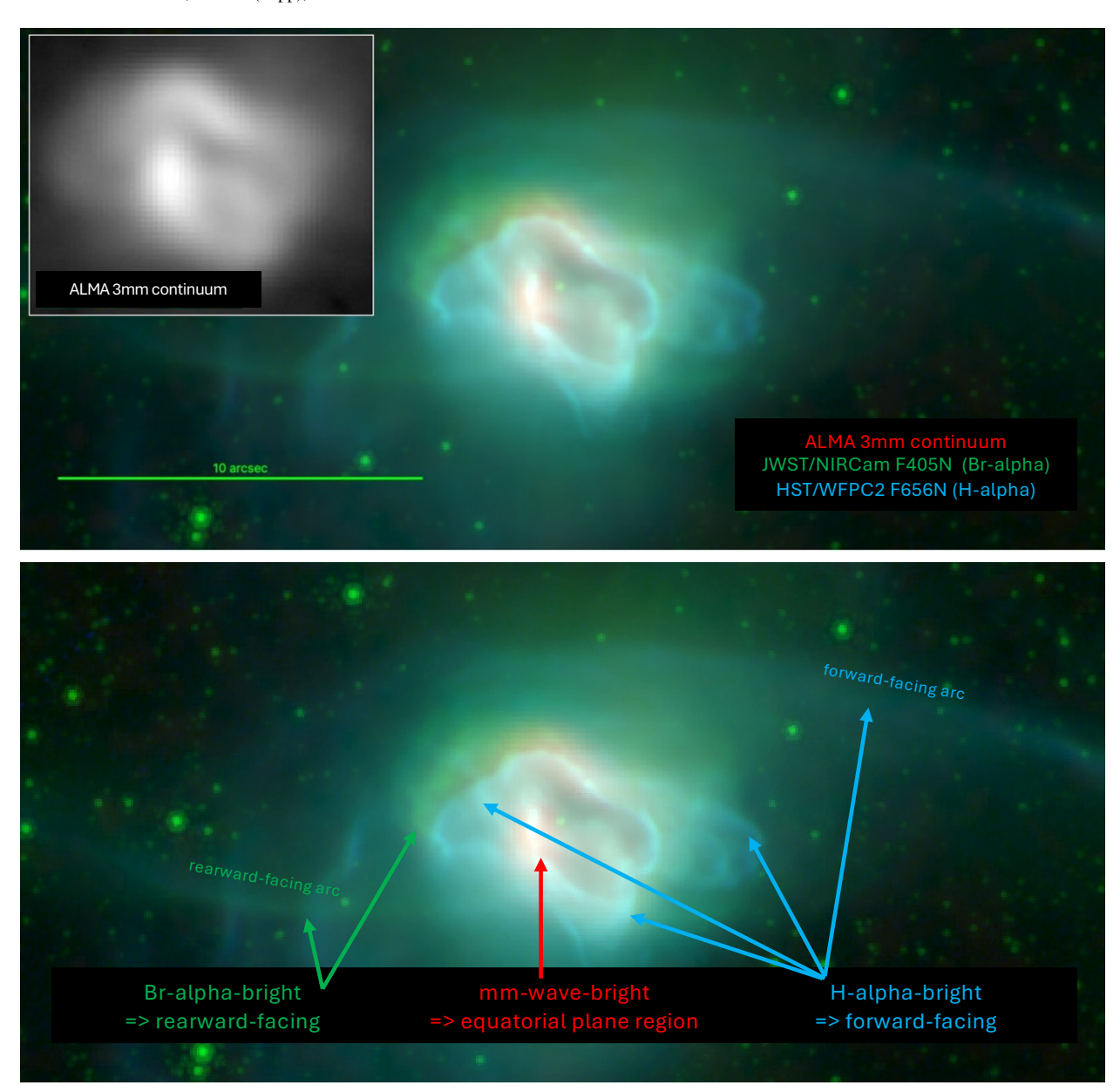


Figure 5. Overlay of ALMA 3 mm continuum emission map (red), JWST/NIRCam  $4.05~\mu m$  Br $\alpha$  image (green), and HST/WFPC2 H $\alpha$  image (blue) of NGC 6537. The ALMA continuum image is also presented in the black and white inset of the top panel. The annotations in the bottom panel denote features that are especially bright in H $\alpha$ , Br $\alpha$ , or 3 mm continuum. Features that are bright in H $\alpha$  or Br $\alpha$  and are likely directed toward and away from the observer, respectively, while the millimeter-wave continuum likely traces ionized material confined to the PN's equatorial plane region (see Section 3.3.1).

map also included (in black and white) as an inset in the top panel of the figure. Annotations in the bottom panel of Figure 5 point out features that are especially bright in  $H\alpha$ , Br $\alpha$ , or 3 mm continuum. The H $\alpha$  emission, being the most susceptible to intranebular extinction, is most likely brightest within the regions of ionized gas that lie in the nebular foreground and are directed toward the observer (cyan-shaded regions in Figure 5); conversely, the Br $\alpha$  emission likely highlights those ionized regions of the nebula that lie in the background and are directed away (green regions in Figure 5). It is hence readily apparent that the three small ( $\sim 3''-5''$  long) lobes or loops of emission near but outside the core that are directed to the east, south-southwest, and west of the central star are foreground/forward-directed features, as is the larger arc of emission extending from the east of the star around to its north and then to its west–northwest. The  $Br\alpha$ -bright diffuse

region extending beyond and to the north of the forward-directed east loop, meanwhile, is directed away, as is the arc feature that wraps around to the south of the star and then to its east—southeast. The two arc features in Figure 5 are evidently the limb-brightened innermost edges of the oppositely directed polar lobes that are imaged in their entirety (in  $H_2$  emission) in Figure 1.

Figure 5 further demonstrates that the 3 mm continuum emission, which is dominated by free-free emission from the ionized gas, traces the central,  $\sim 2''$  radius loop feature within the core (red regions in Figure 5). The millimeter-wave emission from this dense plasma is not susceptible to dust obscuration, and so likely traces ionized gas that is confined to the equatorial plane of the system—a zone sandwiched between, and hence seen projected within, the regions that appear bright in  $H\alpha$  and  $Br\alpha$ . This suggests that the 3 mm

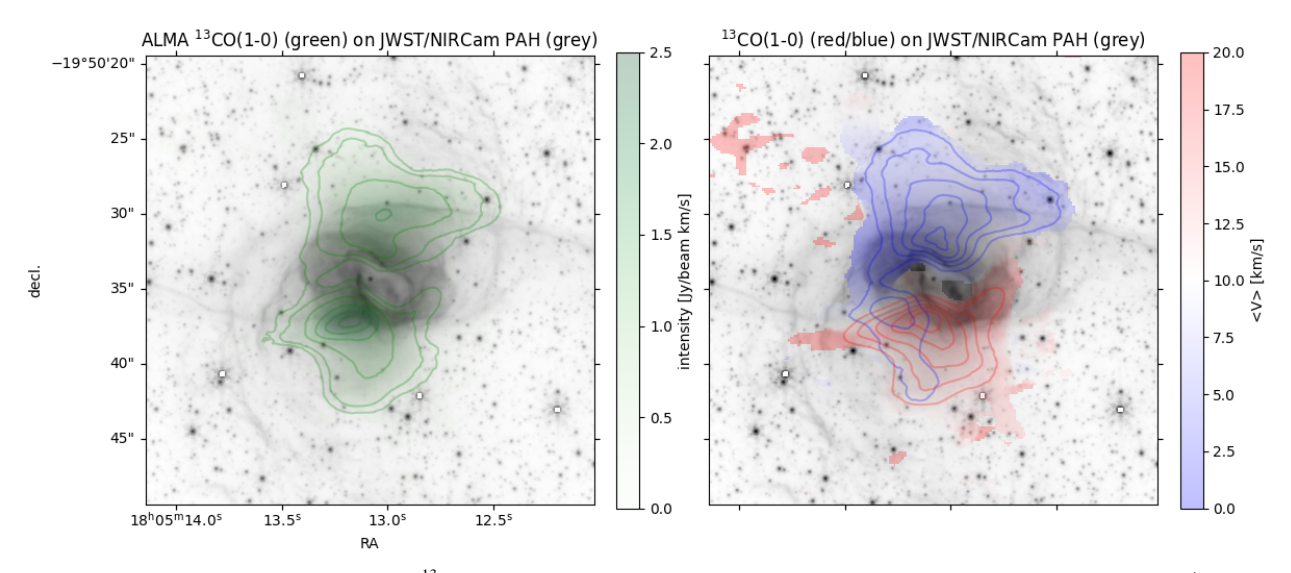


Figure 6. Left: overlay of a velocity-integrated ALMA  $^{13}$ CO(1–0) emission-line map (green linear intensity scale, with green contours) on JWST/NIRCam 3.56 μm PAH imaging (logarithmic gray scale). The contours are set to levels of 0.25, 0.5, 1.0, 1.5, 2.0, and 2.5 Jy beam $^{-1}$  km s $^{-1}$ . Right: intensity-weighted velocity map of ALMA  $^{13}$ CO(1–0) emission, showing blueshifted and redshifted emission (see color bar) on JWST/NIRCam 3.56 μm PAH imaging (gray scale), with contours of velocity-integrated blueshifted (0–9 km s $^{-1}$ ) and redshifted (11–20 km s $^{-1}$ )  $^{13}$ CO(1–0) emission overlaid; the contours are set to levels of 0.25, 0.5, 0.75, 1.0, 1.25, and 1.5 Jy beam $^{-1}$  km s $^{-1}$ .

continuum likely emanates from the ionized innermost regions of the dense, dusty equatorial torus whose outer regions are traced by millimeter-wave emission from <sup>13</sup>CO (see next).

#### 3.3.2. The Molecular Torus

Overlays of the ALMA <sup>13</sup>CO(1–0) image data on the JWST/NIRCam 3.56  $\mu$ m PAH + continuum (F356W) image of NGC 6537 are presented in Figure 6. The left panel illustrates the relationship between the velocity-integrated millimeter-wave <sup>13</sup>CO(1-0) emission and the near-IR PAH and continuum emission. The overlay demonstrates that the cold, dense molecular gas traced by <sup>13</sup>CO is confined to the equatorial regions of the nebula. The 13CO emission in NGC 6537 is also distinctly point symmetric, with bright emission north-northwest and south-southeast of the central star (along PA  $\sim 155^{\circ}$ ) and a conspicuous lack of  $^{13}CO$ emission to its east and west (along PA  $\sim 90^{\circ}$ ). The superposition of <sup>13</sup>CO and PAH + continuum emission also reveals a central cavity in the molecular gas that is spatially coincident with the bright emission from ionized gas at the nebular core (i.e., the emission that dominates Figure 5).

The right panel of Figure 6 reveals the radial velocity field of the  $^{13}\mathrm{CO}(1\text{--}0)$  emission, demonstrating the expansion of the molecular gas from the vicinity of the central star. The data cube and moment 1 (intensity-weighted velocity) image are characterized by a projected expansion velocity of  $V_{\rm exp} \sim 10~{\rm km~s^{-1}}$  with respect to NGC 6537's systemic velocity of  $\sim 10~{\rm km~s^{-1}}$  (J. L. Edwards & L. M. Ziurys 2013). This  $V_{\rm exp}$  is similar to that measured for the low-velocity component of ionized gas in the nebular core (18 km s $^{-1}$ ; L. Cuesta et al. 1995), suggesting the molecular gas and the low-velocity ionized gas are two components of the same physical structure. Surprisingly, however, the blueshifted  $^{13}\mathrm{CO}(1\text{--}0)$  line emission is seen superimposed on the western quadrant of the rearward-facing NE lobe and the redshifted line emission is projected against the eastern quadrant of the forward-facing SW lobe. This unexpected juxtaposition is in fact readily explained if we hypothesize that—as in the case for other, analogous molecular-rich bipolar nebulae

(e.g., NGC 6302; P. Moraga Baez et al. 2025)—the molecular gas is confined to an expanding equatorial torus that is oriented nearly perpendicularly to the main outflow lobes. In the case of NGC 6537, it appears this expanding molecular torus is characterized by a profoundly point-symmetric density structure whose main direction of symmetry, like that of the 1.64  $\mu m$  [Fe II] emission, is significantly out of alignment with the polar axis of the nebula as seen projected against the plane of the sky. Specifically, given the polar lobe axis of symmetry (PA  $\sim 45^{\circ}$ ; Figure 1), the projected orientation of peak  $^{13}CO$  emission (PA  $\sim 155^{\circ}$ ) is evidently rotated by  $\sim 20^{\circ}$  with respect to the expected (projected) orientation of the nebula's equatorial plane (i.e., PA  $\sim 135^{\circ}$ ).

Notwithstanding its point symmetry and misalignment, if we assume the inclination of the molecular torus axis of symmetry with respect to the plane of the sky is identical that of NGC 6537's polar axis (38°; R. L. M. Corradi & H. E. Schwarz 1993), then the deprojected expansion velocity of the torus we obtain from the  $^{13}CO(1-0)$  data is  $\sim 13$  km s<sup>-</sup> From Figure 6, we deduce a projected angular radius of  $\sim 9''$ for the outer edge of the molecular torus, leading to a deprojected linear radius of  $\sim 0.13$  pc assuming D = 1.8 kpc. The implied torus dynamical age—or, more accurately, the time since onset of copious equatorial mass loss—is then  $\sim$ 10,000 yr. This timescale is significantly larger than the  $\sim$ 3700 yr dynamical age of the lobes, given their extents in the JWST H<sub>2</sub> imaging and their deprojected velocities as inferred from ground-based spectroscopy (Section 3.1). Such a disparity in lobe versus torus ages-wherein the relatively slow outflow of dense material along the equatorial plane appears to have been initiated well prior to the formation of the fast outflows that generated the rarefied polar lobes—appears to be a defining characteristic of molecule-rich, bipolar PNe (P. Moraga Baez et al. 2025) and PNe with torus-lobe morphologies more generally (e.g., P. J. Huggins 2007; M. T. García-Díaz et al. 2009). We further consider this aspect of the structural evolution of NGC 6537 in Section 4.

#### 3.3.3. Upper Limits on X-Ray Emission from NGC 6537

The Chandra PN Survey (ChanPlaNS) demonstrated that ~30%-40% of PNe exhibit either diffuse (extended), soft X-ray emission from rarefied, shock-heated gas ("hot bubbles") generated by wind collisions (J. H. Kastner et al. 2012; M. Freeman et al. 2014, and references therein) or a point-like and (typically) somewhat harder X-ray source likely associated with the corona of a putative companion star (R. Montez et al. 2015, and references therein). A subset of these X-ray-detected PNe exhibits both diffuse and point-like X-ray sources. Our nondetection of X-rays in deep Chandra/HRC-I imaging of NGC 6537 (Section 2.2) hence provides constraints on both forms of PN high-energy phenomena associated within this nebula.

To obtain upper limits on the X-ray luminosities of diffuse  $(L_{X,d})$  and point-like  $(L_{X,p})$  sources within NGC 6537, we measured the background counts in the cosmic-ray-screened, 76.13 ks exposure Chandra/HRC-I image within a 40" radius circular aperture centered on the nebula. Within this region, we recover 3131 events, for a background photon count rate of  $8.12 \times 10^{-3}$  counts ks<sup>-1</sup> arcsec<sup>-2</sup>. Applying this result to  $3'' \times 2''$  elliptical ( $\sim$ 18 arcsec<sup>2</sup>) and 1.0 radius circular ( $\sim$ 3 arcsec<sup>2</sup>) regions encompassing the nebular core and central star, respectively (see Section 3.2), yields respective background count rates of  $0.15 \pm 0.05$  ks<sup>-1</sup> and  $0.02 \pm 0.01$  ks<sup>-1</sup>, where the uncertainties reflect Poisson photon counting. The  $5\sigma$  upper limits on source count rates within the ionized core and central star regions implied by our nondetection of X-ray photons from NGC 6537 within these regions are thus  $\sim$ 0.25 ks<sup>-1</sup> and  $\sim$ 0.05 ks<sup>-1</sup>, respectively.

To convert these count rate upper limits to X-ray flux upper limits, we used the webPIMMS<sup>12</sup> spectral modeling tool. We adopt the APEC thermal plasma model, assuming plasma temperatures of 3 MK and 10 MK for the ionized core and central star source regions, respectively. The former is typical of the energetic shocks from collisions between the fast (present-day) central star and ambient ("fossil" AGB) winds (J. H. Kastner et al. 2012; R. J. Montez & J. H. Kastner 2018, and references therein), while the latter are typical of the coronae of active central star companions (R. Montez et al. 2015, and references therein). We further assume an intervening absorbing column of  $N_{\rm H} = 7 \times 10^{21} \, {\rm cm}^{-2}$ , corresponding to extinction toward the central star and nebular core region of  $A_V = 3.7$  (M. Matsuura et al. 2005). For these choices of model parameters, the measured Chandra/HRC-I count rate limits correspond to webPIMMS-inferred upper limits on the intrinsic 0.2-10 keV fluxes of (diffuse) nebular core and (point-like) central star X-ray emission of  $\sim 4 \times 10^{-14}$  erg cm<sup>-2</sup> s<sup>-1</sup> and  $\sim 5 \times 10^{-15}$  erg cm<sup>-2</sup> s<sup>-1</sup>, respectively. These flux limits yield limiting luminosities of  $L_{X,d} \lesssim 1.5 \times 10^{31}$  erg s<sup>-1</sup> and  $L_{X,p} \lesssim 2 \times 10^{30}$  erg s<sup>-1</sup> for the diffuse and point-like X-ray emission sources, respectively, given our assumed distance of 1.8 kpc.

Putting these results into perspective, the upper limit on  $L_{X,d}$  is a factor  $\sim 5$  smaller than the X-ray luminosities of the diffuse X-ray sources within the much younger (dynamical age  $\sim 1000$  yr), molecule-rich PNe NGC 7027 (R. J. Montez & J. H. Kastner 2018) and BD+30°3639 (J. H. Kastner et al. 2000). Our nondetection of X-rays from energetic shocks in NGC 6537 is nevertheless consistent with the results of

ChanPlaNS, which yielded few such detections of diffuse X-ray emission within molecule-rich PNe (J. H. Kastner et al. 2012; M. Freeman et al. 2014). Meanwhile, the upper limit on  $L_{X,p}$  appears to rule out the presence of a close, magnetically active, main-sequence companion star of bolometric luminosity  $L_{\rm bol} \gtrsim 2 \times 10^{33}$  erg s<sup>-1</sup>, corresponding to G or earlier spectral type, that has been spun up to coronal saturation levels (i.e., exhibits  $\log(L_{X,p}/L_{\rm bol}) \sim -3$ ) via accretion of AGB ejecta (R. Montez et al. 2015, and references therein). We stress, however, that the limits on both  $L_{X,d}$  and  $L_{X,p}$  derived here are dependent on the aforementioned choices of parameters (especially plasma temperatures) input to the respective X-ray source models.

# 4. The Structure and Evolution of the Red Spider Nebula

# 4.1. Main Structural Components

In light of the results just presented, we have constructed a schematic view of the main structural components of NGC 6537. This schematic is presented in Figure 7, below a reference color overlay of the JWST/NIRCam  $H_2$ , [Fe II], and  $Br\alpha$  images. The basic structural components, moving inwards, consist of the following.

- 1. A pair of  $H_2$ -bounded polar lobes, with photoionized and/or shock-ionized inner rims, generated by the fast ( $\sim 300$ – $400 \text{ km s}^{-1}$ ) polar flows detected in ground-based long-slit spectroscopy (R. L. M. Corradi & H. E. Schwarz 1993).
- 2. The point-symmetric, [Fe II]-emitting regions along opposing lobe walls, which likely mark the interaction zones where ongoing fast outflows are shearing and shocking the relatively dense, swept up material along the lobe rims.
- 3. A dense and dusty equatorial torus that is slowly expanding (expansion velocity  $\sim 10~{\rm km~s^{-1}}$ ). The torus is primarily composed of cold ( $\lesssim\!100~{\rm K}$ ), CO-emitting molecular gas, but its innermost region is heated and ionized by UV and (perhaps) fast winds from the central star, and is hence a luminous source of H recombination line emission and near-IR and 3 mm continuum (freefree) emission.
- A bubble-like dust structure that appears as a zone of bright PAH emission surrounding the ionized core region.

The line of sight toward this system, indicated at the upper right of the schematic diagram in Figure 7, is such that both the polar axis and the equatorial torus are viewed at intermediate inclination, so as to be consistent with the inferred polar axis inclination ( $\sim 30^{\circ}-40^{\circ}$ ; R. L. M. Corradi & H. E. Schwarz 1993; L. Cuesta et al. 1995).

We note two caveats regarding the structural schematic view of NGC 6537 in Figure 7. First, for simplicity, we have chosen not to include in this illustration a representation of the ionized nebular core itself, with its interior, bright-rimmed, ring or irregular spiral feature, and protruding, bubble-like structures. The JWST imaging of this ionized core region, which likely marks the UV-bathed and fast-wind-heated interior portions of the equatorial torus (Figure 4, middle and bottom panels), is shown as an inset in the color overlay above the schematic diagram. Second, while the approximate line of sight toward this system of structural components (corresponding to the

<sup>12</sup> https://heasarc.gsfc.nasa.gov/cgi-bin/Tools/w3pimms/w3pimms.pl

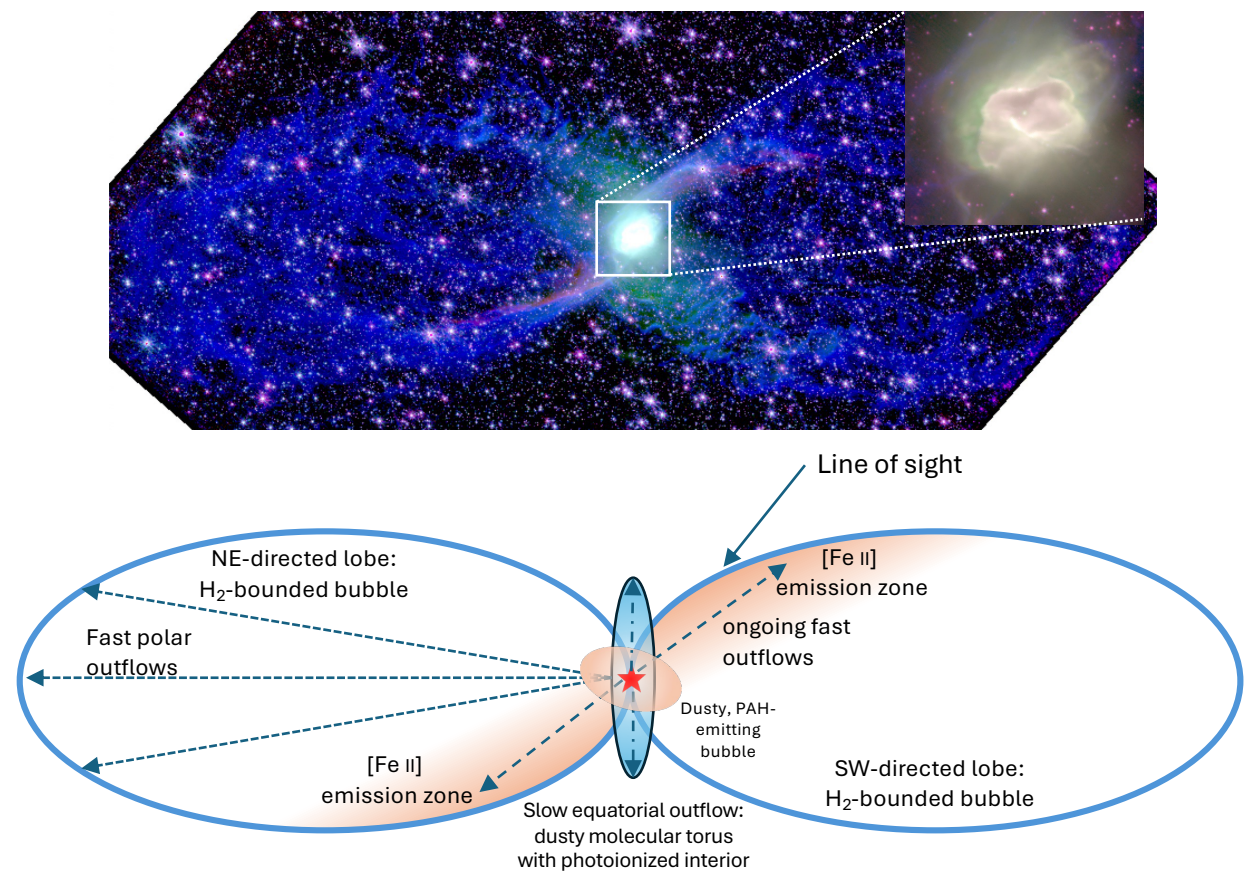


Figure 7. Top: overlay of 4.05  $\mu$ m Br $\alpha$  (green), 2.12  $\mu$ m H<sub>2</sub> (blue), and 1.64  $\mu$ m [Fe II] (red) images of NGC 6537, rotated through 47° in PA (such that the polar axis is horizontal in the image). The inset shows a zoom into the core region, which is saturated in the wide-field rendering. Bottom: schematic of the main structural components of NGC 6537: (1) H<sub>2</sub>-bounded polar lobes; (2) point-symmetric, [Fe II]-emitting regions along opposing lobe walls; (3) slowly expanding equatorial molecular torus with ionized interior; and (4) bubble-like dust structure detected in PAH emission. The line of sight toward the system (indicated at the upper right of the diagram) is such that both the polar axis and the equatorial torus are viewed at intermediate inclination. See text (Section 4.1).

inferred inclination of the nebular polar axis,  $\sim 30^{\circ}-40^{\circ}$ ; R. L. M. Corradi & H. E. Schwarz 1993; L. Cuesta et al. 1995) is indicated in the diagram, the specific alignment of the polar lobe components with respect to each other and the molecular torus in this schematic (re)projected view of NGC 6537 is merely representative. The 3D orientation of these components remains subject to refinement via comprehensive, high-resolution optical and near-IR spectroscopic measurements of their (ionized gas) kinematics.

Those caveats aside, the picture that emerges from the combined JWST/HST/ALMA view of NGC 6537 (represented schematically in Figure 7) is that of a central star system that has formed a bipolar PN via a complex and (evidently) ongoing sequence of stellar mass-loss events. The ejection of the molecular torus, which began ~10,000 yr ago and is characterized by AGB-like expansion velocities, likely marked the termination of the AGB evolutionary stage of the relatively high-mass nebular progenitor. Beginning a few thousand years after the onset of torus ejection, that slow, dense, equatorially directed outflow was succeeded by, and perhaps helped collimate, the fast polar outflows. Furthermore, the point-symmetric shocks that are marked by the extended [Fe II] emission regions along the opposing sides of the polar lobe walls, as well as the sharp-rimmed structures within and around the ionized nebula core, serve as evidence that this fast outflow stage continues at present, and that the main direction

of outflow has precessed or wandered considerably during the epoch of polar lobe formation.

This scenario for the formation and evolution of NGC 6537 is essentially the same as that postulated for NGC 6302, on the basis of HST, ALMA, and JWST observing campaigns targeting the latter bipolar PN (J. H. Kastner et al. 2022; B. Balick et al. 2023; M. Matsuura et al. 2025; P. Moraga Baez et al. 2025), as well as for the Ring and Southern Ring nebulae (NGC 6720 and NGC 3132, respectively), on the basis of JWST and millimeterwave CO observations of these PNe (J. H. Kastner et al. 2024, 2025). In each case, the sequence of slow, dense equatorial outflows followed by fast, collimated polar outflows-which, as noted above (Section 3.3.2), appears to be a common characteristic of PNe with torus-lobe or torus-jet structurespoints to the influence of a binary companion on the mass loss from the central, post-AGB star that has generated the PN. We return to the evidence in favor of such an interacting binary model for NGC 6537 below (Section 4.3).

#### 4.2. Hydrodynamic Modeling

To understand the physical mechanisms that might explain the basic structure of NGC 6537 illustrated in Figure 7, we turn to the recent hydrodynamic simulations of evolved bipolar nebula formation and growth presented in B. Balick et al. (2019, 2020). The reader is directed to those papers for details of the simulations. The basic model consists of fast,

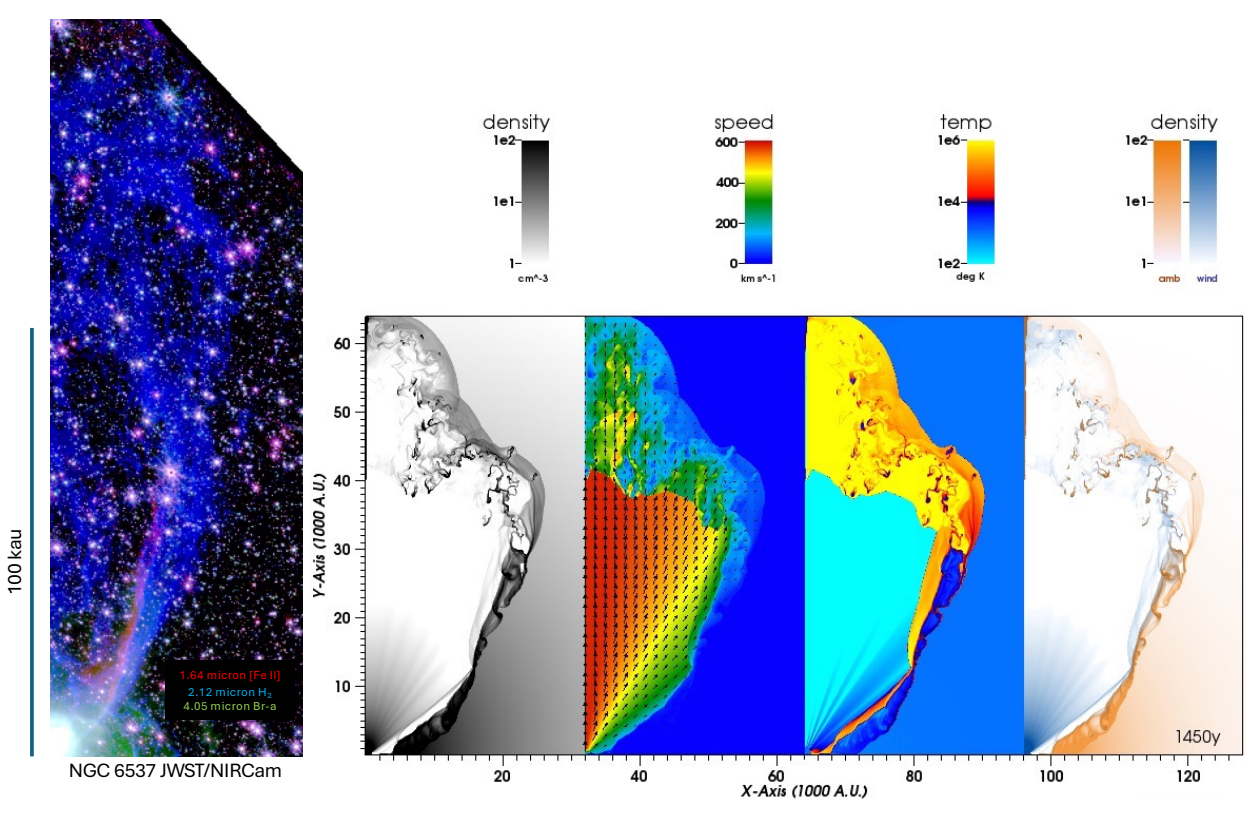


Figure 8. Overlay of 4.05  $\mu$ m Br $\alpha$  (green), 2.12  $\mu$ m H<sub>2</sub> (blue), and 1.64  $\mu$ m [Fe II] (red) images of half of the NE-directed polar lobe of NGC 6537, with the lobe "half" flipped along its polar axis (leftmost panel), compared with images illustrating various aspects of the simulation described in Section 4.2.

azimuthally tapered, post-AGB polar outflows (jets) steadily impinging on slower-moving AGB ejecta whose spherical density profile scales as  $R^{-2}$ . The model is agnostic as to the physical mechanism(s) responsible for the fast outflows and the preexisting AGB outflow.

The specific, simple, two-dimensional simulation presented in Figure 8 is selected as representative of a "family" of simulations included in B. Balick et al. (2019) that appears to match the overall radial and azimuthal appearance of the polar lobes of NGC 6537. The simulation is intended only to be illustrative of the basic physics describing the growth of the polar lobes. The basic parameters of the model include a preexisting and stationary ("slow") AGB wind with a radial density profile given by  $n_{\text{slow}}(r) = 5000 \text{ cm}^{-3} \times (2 \text{ kau}/r)^2$  and a fast wind whose axial density profile is given by  $n_{\text{fast}}(r) = 1000 \,\text{cm}^{-3} \times (2 \,\text{kau}/r)^2$  and axial speed  $v_{\text{fast}} = 600 \,\text{km s}^{-1}$ . Both the density and speed are tapered in the azimuthal direction,  $\theta$ , by a Gaussian whose 1/ewidth is 60°. The diagnostic images in Figure 8 represent the simulation after a duration of 1450 yr, about half the measured kinematic age of the lobes of NGC 6537. At this age, the forward speed of the leading edge of the lobe at  $\theta = 0$  has slowed to 130 km s<sup>-1</sup>, or 25% of the fast-wind ejection speed, owing to the displacement of the denser slow wind downstream. Features along the lobe edges also move far more slowly—at speeds far less than the nearby fast winds whose momentum accelerated them—and their speeds steadily decrease with radius. Thus, in this simulation, the expansion ages of features along the lobe edges can significantly underestimate the time since the onset of the fast wind. Other details concerning the model methodology, as well as the early time structure of the simulation presented here, are described in B. Balick et al. (2022, see their Section 3.3).

A comparison of this representative hydrodynamic model with a NIRCam image overlay for half of the NE polar lobe of NGC 6537 is presented in Figure 8. Notwithstanding the difference in dynamical ages between data and model, it is apparent that the simulation reproduces many of the salient features of the JWST imaging. In particular, the simulated polar lobe opening angles closely match the image data, and the thin edges of the model lobes are closed, highly flocculent (turbulent), and likely perforated, as imaged in  $H_2$ . Moreover, the narrow high-temperature wind interaction region along the inner edge of the lobe walls—which appears red-orange in the rendering of the simulation temperature map, indicative of a gas temperature in the range  $\sim 10^4 - 10^5$  K—closely matches the position and width of the [Fe II]-emitting regions detected by NIRCam.

The comparison in Figure 8 hence supports the basic nebular formation model described schematically in Section 4.1 and Figure 7. We caution, however, that the methodology underlying the simulation illustrated in Figure 8 was not designed to model the physical conditions resulting from a highly directed jet whose outflow direction is likely directionally variable, and is presently (and perhaps persistently) misaligned with the axis of symmetry of the polar lobes, such as appears to be responsible for the [Fe II] emission along opposing lobe walls imaged in NGC 6537 (as well as in NGC 6302; J. H. Kastner et al. 2022). Additional hydrodynamical modeling that is specifically tailored to such a "wandering" polar outflow configuration is clearly warranted.

# 4.3. Infrared Excess at the Central Star: Smoking Gun of Binarity?

To confirm and further investigate the nature of the IR excess of the central star that is evident in Figure 3 as well as

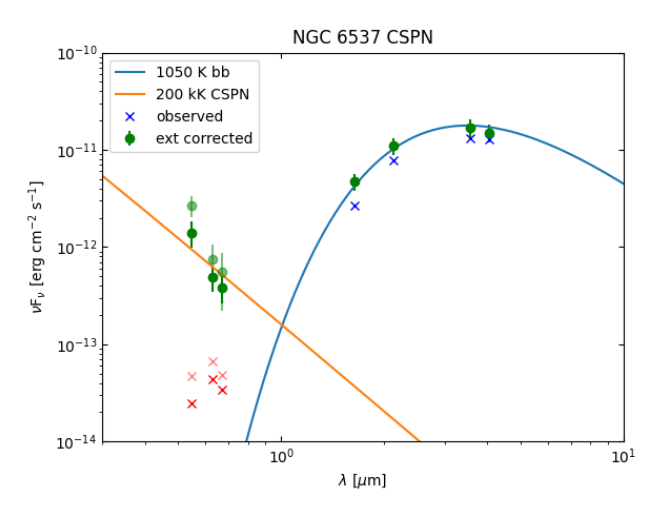


**Figure 9.** SED of the central star of the PN of NGC 6537 from 0.55  $\mu$ m to 4.05  $\mu$ m, as extracted from (archival) HST/WFPC2 and (our new) JWST/NIRCam narrowband images (red and blue × symbols, respectively). Dark and light red × symbols indicate our photometry and photometry reported in M. Matsuura et al. (2005), respectively. The extinction-corrected photometry (assuming  $A_V = 3.7$ ; M. Matsuura et al. 2005) is displayed as green symbols, with dark and light symbols for our results and those reported in M. Matsuura et al. (2005), respectively. The SED is overlaid with blackbodies representing the hot central star photosphere (orange curve) and hot dust (blue curve) that have been (arbitrarily) scaled to the extinction-corrected photometry, for reference.

Figure 4, we extracted photometry for the star from the new JWST/NIRCam and archival HST/WFPC2 images. As the point-spread functions of the HST and JWST images are all <0.3 (FWHM) and are reasonably well matched, we used an aperture of radius of 0.15 and an annulus with inner and outer radii of 0.15 and 0.3 to measure the central star and background fluxes, respectively, within the four JWST/ NIRCam images as well as the HST/WFPC2 F547M, F631N, and F673N filter images. The latter set of (HST) images are those for which the bandwidths are relatively wide and line emission is relatively weak and, hence, the central star is clearly detected (see M. Matsuura et al. 2005). The resulting central star fluxes, corrected for reddening assuming  $A_V = 3.7$ (M. Matsuura et al. 2005), are presented in Figure 9, where we also include the extinction-corrected flux measurements reported in M. Matsuura et al. (2005). The errors in our flux measurements are dominated by uncertainties in the determination of the bright nebular background, and different background subtraction strategies likely account for the slight discrepancies between our photometry and that determined by M. Matsuura et al. (2005).

The resulting 0.55 to 4.05  $\mu$ m SED of the central star of NGC 6537 in Figure 9 clearly demonstrates the presence of a significant IR excess, extending across all four JWST filters. The photospheric temperature of the central star, which is poorly constrained by the HST/WFPC2 data (see M. Matsuura et al. 2005, their Table 3), is represented by a 200 kK blackbody model in the Figure. The IR excess can then be well matched by a model blackbody that peaks at a wavelength of roughly 3.5  $\mu$ m, corresponding to a blackbody temperature of  $\sim$ 1000 K, i.e., approaching dust sublimation conditions. This suggests that the excess IR radiation from the central star's vicinity, if due to thermal emission from dust, emanates from grains heated nearly to the point of sublimation by the luminous central star's intense radiation field. From simple

thermal equilibrium considerations, the emitting dust would lie at a characteristic distance of  $\sim$ 7 au from the star, assuming a stellar luminosity of 8500  $L_{\odot}$  (S. Casassus et al. 2000).

The bipolar PN NGC 6537 thus can be added to the growing list of PNe, most of them molecule rich, for which the central star exhibits an IR excess due to dust in an unresolved or only marginally resolved circumstellar structure—beginning with the detection by the Spitzer Space Telescope of an IR excess at the central star of the Helix Nebula (NGC 7923; K. Y. L. Su et al. 2007) and, in the era of JWST, continuing with detections of IR excesses at the central stars of the Ring and Southern Ring nebulae (NGC 6720 and NGC 3132, respectively; O. De Marco et al. 2022; R. Sahai et al. 2023, 2025) as well as NGC 6537's close analog, NGC 6302 (R. Wesson et al. 2025, in preparation; see also M. Matsuura et al. 2025). In all four cases just mentioned, detections of the PN central star IR excesses required JWST's unique combination of (IR) wavelength coverage and subarcsecond imaging resolution. However, of the four, only the stellar photosphere of NGC 6302 has escaped direct detection by both HST and JWST, as a consequence of the near edge-on orientation of its extensive, optically thick torus (J. H. Kastner et al. 2022; M. Matsuura et al. 2025). In contrast to NGC 6302, and in spite of the many similarities between this nebula and NGC 6537, the photospheric emission of the central star of NGC 6537 is directly detectable and measurable (Figure 9) thanks to the intermediate inclination of its dusty, expanding molecular torus (Figure 7).

Most investigations of PN central star IR excesses have concluded that the circumstellar dust responsible for the excess resides in a long-lived, orbiting disk, most likely in a circumbinary configuration, although the mechanisms that might generate a circumbinary dust disk in evolved star systems remain subject to vigorous debate (see, e.g., G. C. Clayton et al. 2014; O. De Marco et al. 2022; R. Sahai et al. 2025, and references therein). By analogy with the aforementioned previous cases of IR excesses at the central stars of PNe, the most likely explanation for the presence of the compact (unresolved) hot dust source detected within NGC 6537 in our JWST imaging is that the central star resides in a binary system that is orbited by a circumbinary disk.

While such a (Keplerian disk) configuration would appear to stand in stark contrast to the expanding molecular torus we have detected in <sup>13</sup>CO emission (Section 3.3.2) in terms of both size scale and kinematics, these two circumstellar structures may be complementary, rather than contradictory: both point to the influence of a binary companion on the massloss history of the progenitor star of NGC 6537. That is, the same (putative) companion responsible for formation of a dusty circumbinary disk also may have focused the primary's pre-PN (AGB epoch) mass loss along the equatorial plane of the system (e.g., N. Mastrodemos & M. Morris 1999), thereby generating the dusty, molecular torus and the fast, collimated polar outflows that followed torus formation. The fact that the polar outflows in NGC 6537 appear to change direction over time (Section 4.1) is, again, very similar to the variabledirection, point-symmetric outflows observed in NGC 6302 (B. Balick et al. 2023) as well as in many other molecule-rich, bipolar and multipolar PNe that are both dynamically younger (e.g., NGC 7027; P. Moraga Baez et al. 2023) and older (e.g., NGC 6072; S. Kwok et al. 2010). Such wandering or precessing collimated outflows or jets have been proposed as

the natural outcomes of interacting binary systems involving mass-losing AGB stars, either in detached configurations in which the secondary captures a fraction of the AGB primary's ejected mass and forms an accretion disk (e.g., N. Mastrodemos & M. Morris 1998; R. Sahai et al. 2016, and references therein), or in closer configurations that lead to the companion's plunging into the AGB envelope (e.g., N. Soker 2019, and references therein).

#### 5. Summary and Conclusions

We have presented new JWST NIRCam Br $\alpha$ , H<sub>2</sub>, [Fe II], and PAH imaging of the dusty, molecule-rich, pinched-waist, high-excitation bipolar PN NGC 6537 (the Red Spider Nebula). The combination of JWST/NIRCam 4.05  $\mu$ m Br $\alpha$ and archival ALMA 3 mm continuum images provides an extinction-penetrating view of the ionized nebular core, highlighting its complex structure. This ionized core region is shown to consist of a highly asymmetric ring or irregular spiral of radius  $\sim 5''$  ( $\sim 0.04$  pc) with surrounding bubble or loop structures that are superimposed on the inner rims of the nebula's inclined bipolar lobes. Immediately surrounding the ionized core region imaged by JWST and HST is a pointsymmetric, expanding, equatorial molecular torus of projected radius  $\sim 0.08$  pc and projected outflow velocity  $\sim 10$  km s<sup>-1</sup> that is traced by ALMA <sup>13</sup>CO(1–0) emission-line mapping. Assuming the polar axis of the nebula is inclined by 38° with respect to the plane of the sky (R. L. M. Corradi & H. E. Schwarz 1993), the deprojected radius ( $\sim$ 0.13 pc) and expansion velocity ( $\sim$ 13 km s<sup>-1</sup>) of the molecular torus yield a torus dynamical age of  $\sim$ 10,000 yr. The Br $\alpha$  and 3 mm continuum images (as well as archival HST H $\alpha$  imaging) evidently reveal photoionized and/or shock-ionized gas in the interior regions of this dense equatorial torus.

JWST/NIRCam imaging of 2.12  $\mu$ m H<sub>2</sub> emission traces the full extent of the polar lobes, demonstrating that they are in fact closed bubble-like structures with projected extents of  $\sim 100''$  ( $\sim 0.8$  pc). Given the deprojected lobe outflow velocities ( $\sim 300 \text{ km s}^{-1}$ ) and polar axis inclination inferred from optical spectroscopy (R. L. M. Corradi & H. E. Schwarz 1993), their deprojected  $\sim$ 0.9 pc lengths indicate that the lobes have formed over dynamical timescales of  $\sim$ 3700 yr. The H<sub>2</sub>-emitting polar lobe walls lie just outside the ionized lobe rims; these H<sub>2</sub>-emitting outer lobe regions are highly structured, displaying delicate filamentary features indicative of local condensations likely resulting from instabilities in the nebula's significant molecular gas component. The PAH emission closely traces this 2.12  $\mu$ m H<sub>2</sub> emission but, unlike the H<sub>2</sub> emission, the PAH emission displays a rapid drop in surface brightness with distance from the central star, indicating that the PAH and H<sub>2</sub> emission are excited by central star UV and slow ( $\sim$ 10–20 km s<sup>-1</sup>) shocks, respectively. Ionized gas found in the foreground and background regions of the inner lobes is traced by the JWST/ NIRCam Br $\alpha$  image and an archival HST/WFPC2 H $\alpha$  image, respectively.

In striking contrast, the 1.64  $\mu$ m [Fe II] image displays an extended S-shaped morphology, with the [Fe II] emission confined to narrow arcs along the inner eastern and western rims of the NE- and SW-directed lobes. This [Fe II] emission morphology very closely resembles that seen in the similarly extreme (molecule-rich, high-excitation) bipolar PN NGC 6302. As in that case, the [Fe II] in NGC 6537 likely

traces fast ( $\sim$ 100 km s<sup>-1</sup>) shocks from collisions of an active, collimated wind emanating from the vicinity of NGC 6537's central star with slower-moving material forming the polar lobe rims; such a fast wind is indicative of the presence of a close (interacting) companion star. Deep Chandra/HRC-I imaging of NGC 6537 yields no detection of X-rays from these shocks despite the high speeds of the collimated outflows and the presence of the [Fe II] emission, indicating that the diffuse X-ray luminosity of the shocked regions of NGC 6537 is at least a factor  $\sim$  5 smaller than the X-ray luminosities of younger, X-ray-detected PNe that are rich in molecular gas (i.e., BD+30°3639 and NGC 7027; J. H. Kastner et al. 2000; R. J. Montez & J. H. Kastner 2018).

The NIRCam imaging demonstrates that the central star has a near-IR excess, indicating the presence of hot ( $\sim$ 1000 K) circumstellar dust. By analogy with other PNe where such a central star near-IR excess is detected, the dust at NGC 6537's central star(s) may reside in an orbiting disk, most likely in a circumbinary configuration. The putative companion to the central star may also be responsible for the fast, collimated outflows that have inflated the polar lobe bubbles traced by near-IR H<sub>2</sub> emission and are presently generating the S-shaped structure seen in [Fe II] emission. The nondetection of X-rays from the vicinity of the central star by Chandra/HRC-I suggests that any such close companion, if a main-sequence star, is less massive than the Sun.

We present a basic model for the structure and formation of NGC 6537. This model consists of a slow, dense equatorial outflow, ejected  $\sim$ 10,000 yr ago, that was impinged upon by more recent (dynamical age  $\sim 3700$  yr) fast, collimated outflows that are likely both episodic and precessing. This general scenario is supported by a hydrodynamic simulation of nebular growth, incorporating these same basic structural and kinematic components, that appears to well reproduce many of the salient features observed in the JWST and ALMA imaging. We assert that this model for the formation and evolution of NGC 6537 likely applies to most, if not all, molecule-rich, bipolar PNe that are descended from relatively massive progenitors. Such a sequence of slow, dense equatorial outflow followed by fast, collimated polar outflows again points to the profound influence of an interacting binary companion to the central, mass-losing primary star on the primary's late evolution and its mass-loss rate and geometry, with this influence beginning during the AGB stage and continuing through the present epoch.

### Acknowledgments

The authors thank the anonymous referee for valuable comments that improved this paper. Support for this research was provided by Space Telescope Science Institute grant JWST–GO–04571.001–A to the Rochester Institute of Technology (RIT), and by the NSF through the National Radio Astronomy (NRAO) Student Observing Support program via award SOSPADA-009 to the RIT. Research by J.K. and P.M. B. on the molecular content of PNe is further supported by NSF grant AST–2206033 to the RIT. M.S.-G. acknowledges the financial support of I+D+i project PID2023-146056NB-C21, funded by the Spanish MICIU/AEI//10.13039/501100011033 and ERDF/UE. This work is based on observations made with the NASA/ESA/CSA James Webb Space Telescope. The data were obtained from the Mikulski Archive for Space Telescopes at the Space Telescope Science

Institute, which is operated by the Association of Universities for Research in Astronomy, Inc., under NASA contract NAS 5-03127 for JWST. These observations are associated with program #4571. The JWST and HST data presented in this article were obtained from the Mikulski Archive for Space Telescopes (MAST) at the Space Telescope Science Institute; the specific JWST and HST observations analyzed can be accessed via DOI: 10.17909/mvvm-p397 and DOI:10.17909/ z0bw-7m72, respectively. This paper employs a list of Chandra data sets, obtained by the Chandra X-ray Observatory, contained in the Chandra Data Collection DOI: 10.25574/cdc.462. This paper makes use of ALMA data ADS/JAO.ALMA#2018.1.00424.S. ALMA is a partnership of ESO (representing its member states), NSF (USA), and NINS (Japan), together with NRC (Canada), NSTC and ASIAA (Taiwan), and KASI (Republic of Korea), in cooperation with the Republic of Chile. The Joint ALMA Observatory is operated by ESO, AUI/NRAO, and NAOJ. The National Radio Astronomy Observatory is a facility of the National Science Foundation operated under cooperative agreement by Associated Universities, Inc.

Facilities: JWST, HST, ALMA, CXO.

#### **ORCID iDs**

Joel H. Kastner https://orcid.org/0000-0002-3138-8250
Paula Moraga Baez https://orcid.org/0000-00021042-235X
Bruce Balick https://orcid.org/0000-0002-3139-3201
Rodolfo Montez, Jr. https://orcid.org/0000-00026752-2909
Caroline Gieser https://orcid.org/0000-0002-8120-1765
Mikako Matsuura https://orcid.org/0000-0002-5529-5593
Jason Nordhaus https://orcid.org/0000-0002-5608-4683
Miguel Santander-Garcia https://orcid.org/0000-0002-7338-0986

### References

```
Aller, L. H., Hung, S., & Feibelman, W. A. 1999, PNAS, 96, 5366
Ashley, M. C. B., & Hyland, A. R. 1988, ApJ, 331, 532
Balick, B., & Frank, A. 2002, ARA&A, 40, 439
Balick, B., Frank, A., & Liu, B. 2019, ApJ, 877, 30
Balick, B., Frank, A., & Liu, B. 2020, ApJ, 889, 13
Balick, B., Swegel, A., & Frank, A. 2022, ApJ, 933, 168
Balick, B., Borchert, L., Kastner, J. H., et al. 2023, ApJ, 957, 54
Bublitz, J., Kastner, J. H., Hily-Blant, P., et al. 2023, ApJ, 942, 14
Casassus, S., Roche, P. F., & Barlow, M. J. 2000, MNRAS, 314, 657
Chen, Z., Frank, A., Blackman, E. G., Nordhaus, J., & Carroll-Nellenback, J. 2017, MNRAS, 468, 4465
```

```
Clayton, G. C., De Marco, O., Nordhaus, J., et al. 2014, AJ, 147, 142
Corradi, R. L. M., & Schwarz, H. E. 1993, A&A, 269, 462
Cuesta, L., Phillips, J. P., & Mampaso, A. 1995, A&A, 304, 475
De Marco, O. 2009, PASP, 121, 316
De Marco, O., Akashi, M., Akras, S., et al. 2022, NatAs, 6, 1421
Edwards, J. L., & Ziurys, L. M. 2013, ApJL, 770, L5
Feibelman, W., Aller, L. H., Keyes, C. D., & Czyzak, S. J. 1985, PNAS,
Freeman, M., Montez, R., Jr., Kastner, J. H., et al. 2014, ApJ, 794, 99
Frew, D. J., Parker, Q. A., & Bojičić, I. S. 2016, MNRAS, 455, 1459
García-Díaz, M. T., Clark, D. M., López, J. A., Steffen, W., & Richer, M. G.
  2009, ApJ, 699, 1633
García-Segura, G., Ricker, P. M., & Taam, R. E. 2018, ApJ, 860, 19
García-Segura, G., Taam, R. E., & Ricker, P. M. 2022, MNRAS, 517, 3822
Gieser, C., Beuther, H., Semenov, D., et al. 2023, A&A, 674, A160
Huang, P.-S., Lee, C.-F., & Sahai, R. 2020, ApJ, 889, 85
Huggins, P. J. 2007, ApJ, 663, 342
Jones, D., & Boffin, H. M. J. 2017, NatAs, 1, 0117
Kastner, J., Moraga Baez, P., Bublitz, J., et al. 2023, AAS Meeting, 241,
Kastner, J. H., Weintraub, D. A., Gatley, I., Merrill, K. M., & Probst, R. G.
  1996, ApJ, 462, 777
Kastner, J. H., Soker, N., Vrtilek, S. D., & Dgani, R. 2000, ApJL, 545,
Kastner, J. H., Montez, R. J., Balick, B., et al. 2012, AJ, 144, 58
Kastner, J. H., Moraga Baez, P., Balick, B., et al. 2022, ApJ, 927, 100
Kastner, J. H., Wilner, D. J., Moraga Baez, P., et al. 2024, ApJ, 965, 21
Kastner, J. H., Wilner, D. J., Ryder, D., et al. 2025, ApJ, 981, 46
Kim, Y., Koo, B.-C., Pyo, T.-S., et al. 2024, MNRAS, 528, 4657
Kraft, R. P., Nulsen, P., Tremblay, G., et al. 2018, Proc. SPIE, 10699,
Kwok, S., Chong, S.-N., Hsia, C.-H., Zhang, Y., & Koning, N. 2010, ApJ,
  708, 93
Marquez-Lugo, R. A., Ramos-Larios, G., Guerrero, M. A., & Vázquez, R.
  2013, MNRAS, 429, 973
Mastrodemos, N., & Morris, M. 1998, ApJ, 497, 303
Mastrodemos, N., & Morris, M. 1999, ApJ, 523, 357
Matsuura, M., Zijlstra, A. A., Gray, M. D., Molster, F. J., &
  Waters, L. B. F. M. 2005, MNRAS, 363, 628
Matsuura, M., Volk, K., Kavanagh, P., et al. 2025, MNRAS, 542, 1287
Montez, R., Jr., Kastner, J. H., Balick, B., et al. 2015, ApJ, 800, 8
Montez, R. J., & Kastner, J. H. 2018, ApJ, 861, 45
Moraga Baez, P., Kastner, J. H., Bublitz, J., et al. 2023, AAS Meeting, 55,
  468.02
Moraga Baez, P., Kastner, J. H., Bublitz, J., et al. 2025, ApJ, submitted
Morris, M. 1987, PASP, 99, 1115
Quireza, C., Rocha-Pinto, H. J., & Maciel, W. J. 2007, A&A, 475, 217
Rowlands, N., Houck, J. R., & Herter, T. 1994, ApJ, 427, 867
Sabin, L., Zijlstra, A. A., & Greaves, J. S. 2007, MNRAS, 376, 378
Sahai, R., Scibelli, S., & Morris, M. R. 2016, ApJ, 827, 92
Sahai, R., Bujarrabal, V., Quintana-Lacaci, G., et al. 2023, ApJ, 943, 110
Sahai, R., Van de Steene, G., van Hoof, P. A. M., et al. 2025, ApJ, 985, 101
Soker, N. 2019, MNRAS, 483, 5020
Soker, N., & Livio, M. 1994, ApJ, 421, 219
Soker, N., & Rappaport, S. 2000, ApJ, 538, 241
Su, K. Y. L., Chu, Y. H., Rieke, G. H., et al. 2007, ApJL, 657, L41
Zou, Y., Frank, A., Chen, Z., et al. 2020, MNRAS, 497, 2855
```